ACS OMEGA

http://pubs.acs.org/journal/acsodf

Article

Fabrication of Alkaline Electrolyzer Using Ni@MWCNT as an Effective Electrocatalyst and Composite Anion Exchange Membrane

Dimple K. Bora, Priyanka P. Bavdane, Vidhiben Dave, Sooraj Sreenath, Govind Sethia, Ashis Kumar Satpati, and Rajaram K. Nagarale*

Cite This: *ACS Omega* 2022, 7, 15467−15477

Read Online

ACCESS | Metrics & More | Article Recommendations | Supporting Information

ABSTRACT: Here, we report the synthesis of nickel nanoparticles thermally encapsulated in multiwalled carbon nanotubes (MWCNTs) and its utility in alkaline water splitting by combining with composite thermoset anion-exchange membrane. Ni@MWCNT displayed both oxygen evolution reaction (OER) and hydrogen evolution reaction (HER). It provided 10 mA cm^{-2} current density at an overpotential of 300 mV for OER and 254 mV for HER on a glassy carbon electrode, respectively. Base-catalyzed N-methly-4-piperidone-formaldehyde-based prepolymer was grafted on to poly(vinyl alcohol) and cross-linked via thermal annealing followed by quaternization using methyl iodide to obtain thermoset anion exchange membrane (NMPi). Composite NMPi membranes were synthesized using additives tetraethyl orthosilicate (TEOS) and zirconium oxychloride. The water splitting performance on the fabricated membrane electrode assembly was tested and compared with commercially available Neosepta membrane. The obtained faradic efficacy of the water splitting was 94.33% for ZrO_2-NMPi membrane followed by 80.23%, 77.70%, and 65.10% for SiO_2-NMPi, NMPi, and Neosepta membranes, respectively. The best membrane ZrO_2-NMPi achieved maximum current density of ~0.776 A cm^{-2} in 5 M KOH electrolyte at 80 °C and 2 V applied constant voltage. The excellent alkaline stability of MEA indicates its potential utility in hydrogen generation applications.

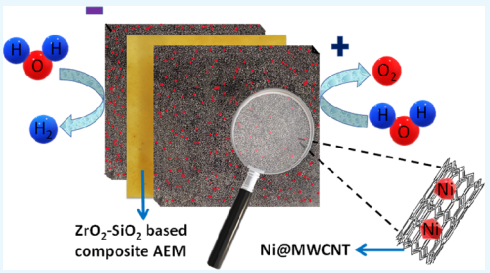

INTRODUCTION

Electrochemical water splitting establishes a potential route to generate and store renewable energy.[1−5] However, high thermodynamics and sluggish reaction kinetics of the electrode hinder practical applications. The typical operating voltage of the commercial electrolyzer is ~1.8−2.0 V, which is far higher than the 1.23 , thermodynamic potential of the water splitting.[6,7] The factors contributing to high water splitting potential are activation energy, diffusion of ions on electrode surface and/or ion mobility in electrolyte, change in concentration near the electrode surface, ohmic resistance of the system, resistance incurred from bubble formation due to blockage of electrode surface, and entropy. The high potential, that is, overpotential and hence the energy efficiency can be minimized by selecting appropriate electrocatalyst which could accelerate oxygen and hydrogen evolution reactions (OER and HER).[7,8] The best known electrocatalysts are noble group elements, precisely Ru, Ir, and Pt metals and their oxides. RuO_2 and IrO_2 exhibit the highest OER activity in alkaline solution, whereas Pt exhibits the highest HER activity in acidic environment.[9] However, their scarcity in the earth's crust and hence the price is the major obstacle. Iridium, the most preferred anode, is one of the rarest elements in the Earth's crust, having an average mass fraction of 0.001 ppm in crustal rock. Conversely, gold and platinum are 40 times and 10 times more abundant, respectively. Further, performance of noble metal catalysts is a mismatch due to their activity in different pH conditions in which they are more stable and most active.[10−12] Hence, the work on nonplatinum group (NPG) metals have attracted tremendous attention in recent years to develop a highly active and robust bifunctional electrocatalyst for sustainable development of clean energy.

The design of new catalyst is based on the theoretical evaluation of "activity volcano" proposed by Man et al. for OER and Roger for HER.[13,14] Of the known transition metal-based catalysts, Ni (or Co) and NiO (or Co_3O_4) based catalysts show high activity for water splitting because of their activity near the peak of the "activity volcano".[7,11,15] The mechanism of OER in alkaline conditions involves the formation of metal−OH bond (M−OH) by a single electron oxidation of hydroxide ions adsorbed on the active surfaces. It is followed by the formation of the M−O bond with coupled electron and proton transport. The M−O combines to form the O_2 by combination of 2 M−O or with the formation of M−OOH followed by the single electron oxidation and

Received: January 4, 2022
Accepted: March 24, 2022
Published: April 27, 2022

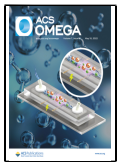

https://doi.org/10.1021/acsomega.2c00070
ACS Omega 2022, 7, 15467−15477

another coupled electron and proton transport pathway to generate O_2.[16,17] The mechanism of HER involves the combination of Volmer step, Heyrovsky step, and Tafel step, and they can be presented as hydronium ion (H_3O^+) discharge and formation of adsorbed (H°_{ad}) on active sites (●) as shown in eqs 1−4[17,18]

In acidic medium

$$(H_3O^+ + \bullet + e^- \rightarrow H^\circ_{ad} + H_2O)\ \text{(Volmer step)} \quad (1)$$

$$(H_3O^+ + H^\circ_{ad} + e^- \rightarrow \bullet + H_2 + H_2O)\ \text{(Heyrovsky step)} \quad (2)$$

$$2H^\circ_{ad} \rightarrow 2\bullet + H_2\ \text{(Tafel step)} \quad (3)$$

In basic medium, H°_{ad} is formed by dissociation of water.

$$H_2O + \bullet + e^- \rightarrow H^\circ_{ad} + OH^- \quad (4)$$

The rate-determining step is the rate of H_{ad} combination and H_2O dissociation. With nickel (Ni) being the most promising HER catalyst, the rate of adsorption of H atom to facilitate the HER was carried out by nickel nanoparticles in carbon or heteroatom-doped carbon materials. In the past few years, there is tremendous interest in Ni-based electrocatalysts for water splitting in alkaline medium.[11,19,20] Yan et al. reported the in situ growth of Ni nanoparticle-encapsulated N-doped carbon nanotubes with 134 mV overpotential for HER.[21] Carbon fiber cloth embedded nickel nanoparticles showed 131 mV overpotential.[22] The nickel anchored porous carbon is also reported.[23] Chhetri et al. reported the HER activity of Ni/$Ni(OH)_2$/graphite electrode with 200 mA cm^{-2} at an overpotential of 0.3 V comparable to platinum (0.44 V).[24] Graphene oxide loaded Ni and NiO nanoparticles showed enhanced HER catalytic activity.[25] The motivation for the anchoring of nickel nanoparticle to carbon matrix is to reduce catalyst leaching during the operation and it promotes the adsorption of H atom to facilitate the HER.

Thermal encapsulation of functional materials in carbon nanotubes is a promising method to anchor catalyst. It was first demonstrated by Ajayan and Ijima by thermal migration of molten metal particles inside the high-temperature-treated carbon nanotubes (CNT);[26] many reports are available on thermal encapsulation of the small organic molecules, metal particles, fullerenes, and metal oxides.[27−31] The formation of "peapod" like structures by encapsulation of fullerenes in CNT was reported by Kataura et al.[32] The molecular electronic application of organic molecules encapsulated CNTs was reported by Takenobu et al.[27] Encapsulation of functionalized endohedral fullerenes inside the thin layered CNT was reported where the complex dynamic behavior of the intercalants was identified.[33] Ugarte et al. proved thermal intercalation of the molten silver particles inside the CNTs by capillary forces and the decomposition of silver nitrate inside the nanotubes to form the chains of the silver nanobeads.[34] In our earlier report, we demonstrated the thermal encapsulation of polyoxometalates in multiwalled carbon nanotubes (MWCNTs) and their application for a nongassing electro-osmotic pump.[35] Here, we have demonstrated a low-temperature thermal encapsulation of Ni nanoparticles in MWCNTs, and its utility as an efficient alkaline water-splitting catalyst by making membrane electrode assembly (MEA).

MEA consist of sandwich of polymeric membrane in between two electrodes (cathode and anode). Membranes used for alkaline water splitting are anion exchange membranes, conducting OH^- ion with a quaternary ammonium functional group.[36] Several quaternary ammonium functionalized polymers such as poly(arylene ether sulfone), poly(phenylene oxide), poly(ether sulfone ketone), and poly(vinyl alcohol) have been reported. It has been well reported that quaternary ammonium cations are generally sensitive toward β-hydrogen elimination (Hoffman degradation) and/or direct nucleophilic substitution (SN2) under alkaline conditions.[37] Therefore, development of new AEM's with dedicated focus on its thermal and mechanical stability in alkaline media has been a serious concern. *N*-methyl piperidone-based AEM prepared by a super acid catalyst has been reported with excellent alkaline stability. Here, we are reporting the base-catalyzed preparation method of *N*-methyl piperidone-based composite AEM and its MEA with thermally encapsulated Ni@MWCNTs for alkaline water splitting.

EXPERIMENTAL SECTION

Material and Methods. Poly(vinyl alcohol) (PVA) Mw 89 000−98 000, 99+% hydrolyzed, tetraethyl ortho silicate (TEOS) ≥ 99.0%, and *N*-methyl-4-piperidone (NMPi) were purchased from Sigma-Aldrich; sodium hydroxide (NaOH) of AR grade, zirconium oxychloride, formaldehyde 37% in water, and nickel(II) acetate ($Ni(OCOCH_3)_2{\cdot}4H_2O$) were sourced from SD Fine Chemicals, India. Graphite paper was purchased from Nikunj Exim Enterprise Ltd. Nickel foam (NF) was purchased from Research Supporters India. Hydrazine monohydrate ($N_2H_4{\cdot}H_2O$), MWCNTs were obtained from SRL, and Nafion dispersion (5 wt %) was procured from Alfa Aesar. All chemicals were used as received without further purification. Ultrapure (deionized) water was utilized during the experiments.

Synthesis of NMPi Membranes. Briefly, 5 mL of NMP was added in a round-bottom flask containing 12 mL of formaldehyde. To the mixture, 4 mL of 40% NaOH was added dropwise with constant stirring at 0 °C to obtain a clear red color solution, followed by the addition of 100 mL of 10% PVA solution. After 10 min, 10 wt % of TEOS and 10 wt % of zirconium oxychloride with respect to NMP were added and kept for 6 h stirring at room temperature. The resulting reaction mixture was casted on a glass plate, and membrane was obtained via solvent evaporation. The completely dried membrane was peeled off from the glass plate and thermally cross-linked in a muffle furnace at 140 °C for 4 h. The obtained membrane was activated in 1 M HCl and 1 M NaOH alternatively and stored in salt solution. The membrane with TEOS additive was designated as SiO_2-NMPi, the membrane with TEOS and zirconia additives was designated as ZrO_2-NMPi, and the membrane with no additives was labeled as NMPi

Synthesis of Ni@MWCNT. In brief, 100 mg of MWCNTs was heated at 300 °C for 0.5 h in a preheated muffle furnace. The hot MWCNTs was dispersed in 4 mM of nickel acetate solution and stirred for 0.5 h. It followed by the addition of 19 mM of hydrazine monohydrate with continuous stirring for further 1 h. The resulting solution was transferred to a 50 mL Teflon-lined stainless steel vessel and autoclaved at 110 °C for 24 h in a preheated oven. After 24 h, the product was centrifuged and collected through washing with distilled water three times and dried at 60 °C overnight. The prepared material was designated as Ni@MWCNT.

Fabrication of Membrane Electrode Assembly. The nickel foam coated with Ni@MWCNT were used as a cathode

https://doi.org/10.1021/acsomega.2c00070
ACS Omega 2022, 7, 15467−15477

and anode for membrane electrode assembly. The nickel foam of dimensions 5 cm × 5 cm was dipped in 1 M HCl for 10 min and rinsed with distilled water followed by ultrasonication in acetone for 5 min. The nickel foam was washed with distilled water and dried in a vacuum oven overnight prior to use. The catalyst ink was painted on the pretreated nickel foam with a brush coating technique and dried in a vacuum oven at 60 °C for 1 h. The coated nickel foam was hot pressed against the membrane and placed between gaskets of thickness 0.8 mm and inserted between the graphitic plates and clamped hand tightly together with the nuts and bolts. The cell had a provision for feeding the reactant and removal of the products. The two terminals of the cell were connected to the DC supply unit having constant current and constant voltage provisions. The potassium hydroxide solution having a concentration 1 M was pumped across the two compartments of the cell with the help of a pump at a flow rate of 15 mL min^{-1}. The voltage was varied linearly and the corresponding current was measured three times with different time interval to check the reproducibility of the results. The amount of current produced and the voltage applied is monitored with the help of the multimeter.

Characterization. *Membrane Characterization.* 1H NMR spectra were recorded on Bruker DMX-300 NMR instrument at 300 Hz in deuterated DMSO-d^6 solvent. The surface morphology and structural analysis of the synthesized membranes were thoroughly characterized using various analytical tools. X-ray diffraction of the membranes were recorded, and the chemical functionalities were analyzed by Fourier-transform infrared (FTIR). The spectra were recorded on Agilent, Cary 600 series FTIR microscope (with a resolution of ±4 cm^{-1} and incident angle of 45°) in the wavenumber range of 400−4000 cm^{-1}. The thermal characteristics of the membrane was analyzed using thermogravimetric analysis (TGA), TA Instruments 2960 (Mettler Toledo, Germany) at a heating rate of 10 °C min^{-1} from 30 to 800 °C in N_2 atmosphere. The detailed physicochemical and electrochemical characterization of the membranes are presented in Supporting Information.

RESULTS AND DISCUSSION

The successful formation of Ni@MWCNT was confirmed by powder XRD as shown in Figure 1. The XRD profile validate the presence of face-centered cubic (fcc) nickel nanoparticles (JCPDS file: No. 03-1051) with a small diffraction peak of graphite (002) at ∼26° from MWCNTs.[38,39] We could not observe the peak for nickel carbide of the cementite phase and nickel oxides in the diffraction pattern. The results clearly indicate the formation of nickel nanoparticles by thermal migration of nickel ions by capillary suction in the interior and interlayers of MWCNTs followed by its reduction in the presence of hydrazine monohydrate and to form particles by agglomeration. The formation of nickel nanoparticles by reduction with carbon in inert atmosphere has been reported by Koltypin et al. at 500 °C.[40] The formation of micron-sized particles from the reduction of nickel oxide in the presence of natural graphite at 950 °C has also been reported.[41] The broadening of nickel peaks in the XRD pattern is due to its small particle size. The size of the nickel nanoparticles was calculated using the Scherer equation, that is, $t = 0.9\lambda/B \cos \theta B$, where t is the particle size, λ is the characteristic wavelength of the X-ray used, B is the angular width in radians at an intensity equal to half of the maximum peak intensity, and θB the Bragg angle in degrees at which the diffraction occurs.[42] The average particle size of the deposited nickel nanoparticles was estimated as 19 nm, calculated from the Scherer equation using nickel (111) peak at 2θ of 44.5°. This size generally accords to TEM observations (Figure 2).

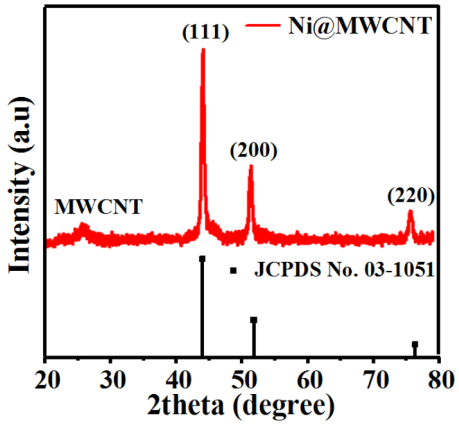

Figure 1. XRD pattern of the Ni@MWCNTs showing the presence of fcc nickel nanoparticles along with JCPDS data.

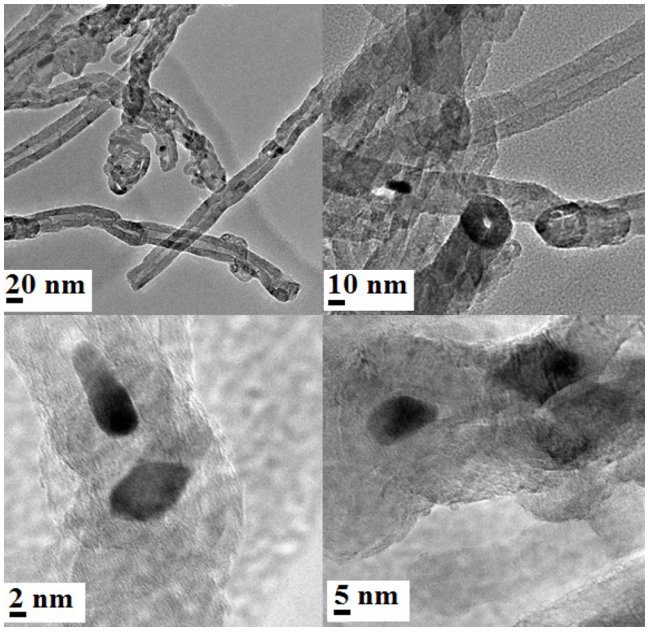

Figure 2. TEM images of Ni@MWCNTs showing encapsulated nickel nanoparticles of irregular shape and size inside the cavities and openings of MWCNTs.

The crystallite of irregular size and shape were observed inside the cavities and at the opening of the MWCNTs. Also, Ni@MWCNT possesses a high BET surface area of 20.7255 ± 0.1585 m^2/g which is represented by the isotherm linear plots (Figure S1). For comparison purposes, BET surface area of neat nickel particles synthesized by reduction of nickel acetate was recorded, and its surface area was found to be 0.0224 ± 0.0120 m^2/g, which is very low compared to Ni@MWCNT.

Figure 3A−C shows the SEM images of encapsulated MWCNTs with elemental mapping and energy dispersive X-ray spectrum. The presence of clear images without aggregation or dirt formation indicated encapsulation inside

https://doi.org/10.1021/acsomega.2c00070
ACS Omega 2022, 7, 15467−15477

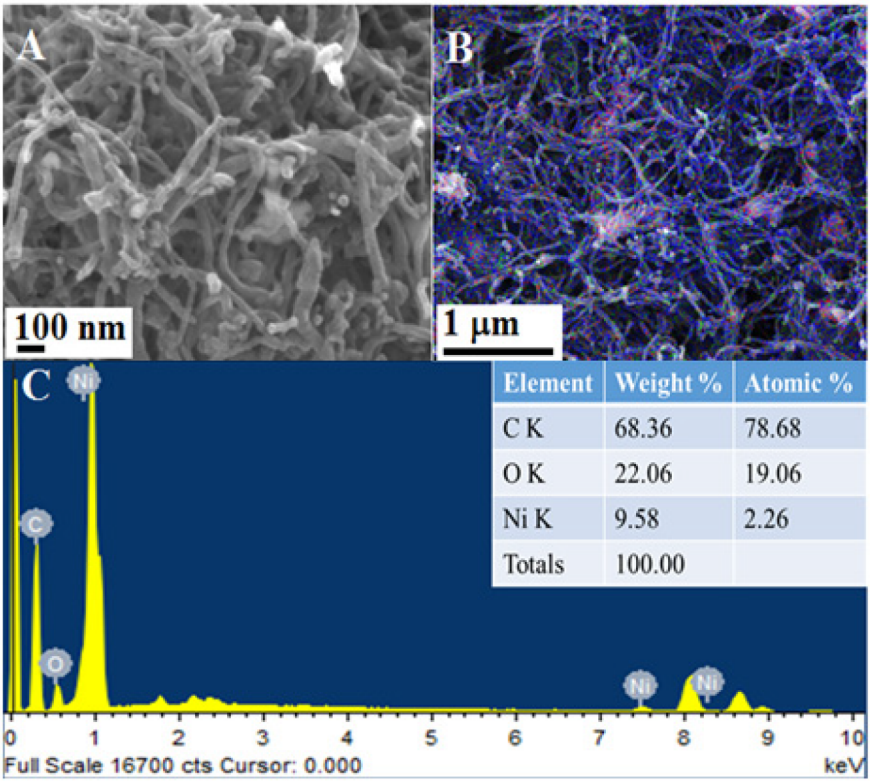

Element	Weight %	Atomic %
C K	68.36	78.68
O K	22.06	19.06
Ni K	9.58	2.26
Totals	100.00	

Figure 3. (A) SEM image of the Ni@MWCNTs showing uniform distribution of Ni nanoparticles. (B) Elemental mapping shows distribution of Ni nanoparticles. (C) Energy dispersive X-ray spectrum showing atomic and weight percentage of Ni.

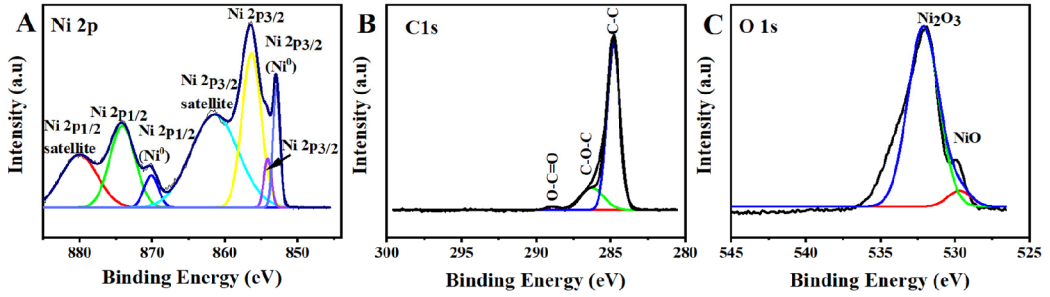

Figure 4. XPS spectra of Ni@MWCNT confirming the presense of metallic Ni°. (A) Ni 2p, (B) C 1s, and (C) O 1s.

the MWCNTs. SEM mapping (Figure 3B) shows the expected nickel element throughout the image suggesting its encapsulation. The energy dispersive X-ray spectrum as shown in Figure 3C confirmed ~9.58 weight% of nickel.

The XPS spectra (Figure 4) was recorded to determine the oxidation state of Ni in Ni@MWCNT. The spectra were deconvoluted to obtain the Ni 2p fitting (Figure 4A). The intense peak at 852.93 and 870.28 eV binding energy indicated the metallic (Ni^0) phase.[43] The peak at 856.53 and 854.34 eV attributed to Ni^{3+} and Ni^{2+} 2p spin orbits.[43,44] The peaks at 861.98 and 880.68 eV represented the satellite peaks for the Ni $2p_{3/2}$ and Ni $2p_{1/2}$ region, respectively.[45,46] The binding energy at 874.38 eV was ascribed to the Ni $2p_{1/2}$ region. The C 1s high-resolution spectra (Figure 4B) showed the intense peak at the binding energy 284.8, 286.43, and 289.0 eV ascribed to the C−C bond, C−O−C bond and O−C═O bond, respectively.[47] The peaks at 531.92 and 529.68 eV observed from the O 1s spectra (Figure 4C) represented the Ni_2O_3 and NiO, respectively, due to surface oxidation during the analysis.[44]

Electrochemical Study. The electrochemical study was performed with paste consisting of 4:1 ratio Ni@MWCNT and Nafion dispersion drop coated on a glassy carbon electrode as the working, Ag/AgCl as the reference, and a glassy carbon rod as the counter electrode in 1 M KOH. The recorded polarization curves for HER and OER are presented in Figure 5 along with the Tafel slope as the insets. In the polarization curve, we could observe the broad oxidation peak in the potential range of 1.25−1.45 V versus RHE, this peak belongs to transformation from NiO to NiOOH (Figure 5B). It is well reported in the literature that the oxidized state of the transition metal is conductive for OER reaction.[7,48] Thus, the more positive the potential of the scan was, the higher the oxidation current was observed. The broadening of the peak indicated a large amount of charging during the anodic potential scan, which is related to the enhanced redox active sites for OER. By scanning the potential further toward the onset potential for the water oxidation, the redox active site, especially the Ni^{3+} redox species, tends to accept the electron released from water during oxidation and regenerated back to

https://doi.org/10.1021/acsomega.2c00070
ACS Omega 2022, 7, 15467−15477

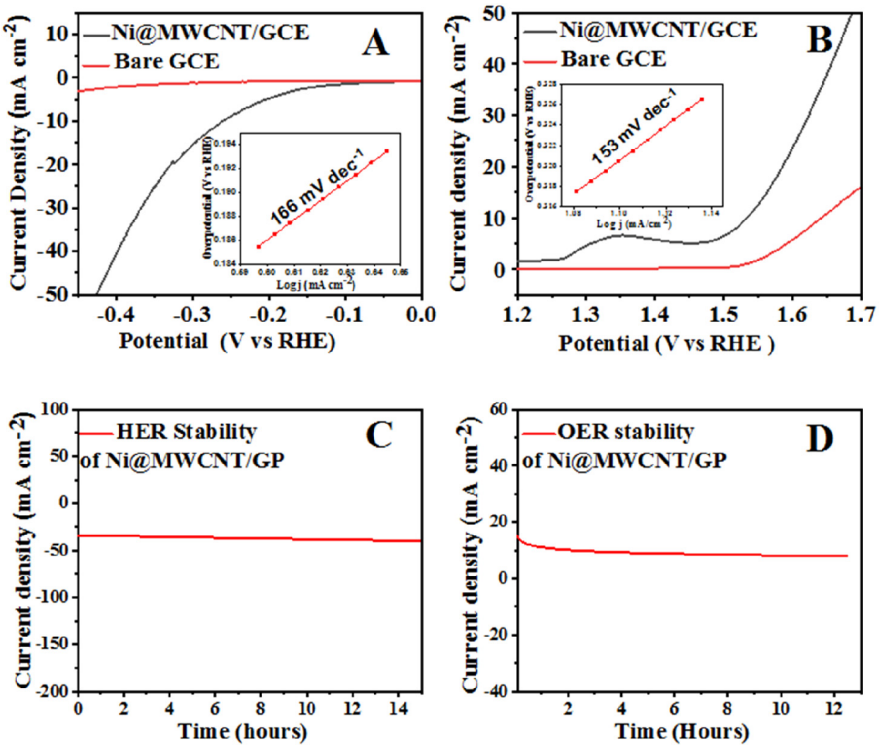

Figure 5. Linear sweep voltammogram of the paste consisting of 4:1 ratio of Ni@MWCNTs and Nafion dispersion drop coated on a glassy carbon electrode as the working, Ag/AgCl as the reference, and a glassy carbon rod as the counter electrode in 1 M KOH with 5 mV scan rate. The normalized current density and potentials were presented versus hydrogen electrode. (A) HER and (B) OER. Insets show the corresponding Tafel slope. (C,D) Stability of the electrode at constant potential for HER and OER respectively.

Ni^{2+} redox state. Thus, the water oxidation process is facilitated with a decrease in the onset potential and enhancement in the oxidation current density.

The observed onset potential of 1.53 V versus RHE being more negative than Ni@C reported.[10,19,22] It was about 100 mV positive than the transition bimetallic catalyst on carbon.[20] We propose that the OER activity is due to the stabilization of intermediate NiO/NiOOH oxidation state by MWCNTs. In our earlier report, we have showed that cations of mixed valence at surfaces of metal oxide nanoparticles constitute electrochemical half-cells with potential intermediates between those of the dissolved cations and those in the solid.[49] The stabilization of polyoxometalates inside the MWCNTs by transfer of electron from MWCNTs to encapsulated polyoxometalates is also reported.[35] Here, we are also anticipating good electron transport from MWCNTs to encapsulated nickel nanoparticles to stabilize the intermediate oxidation state which is responsible for good OER activity. Furthermore, the conducting MWCNTs enhanced fast charge transport which is beneficial to increase reaction efficiency. The formation of metal/p-type semiconductor, that is, Ni@MWCNT can generate a positive space charge region on the metal surface which can further promote the OER activity.[18] The well distributed nickel nanoparticles with high surface area allowed the high mass transport, that is, transport of OH^- and O_2 to commence the ease of OER activity. The observed over potential and Tafel slope were 300 mV and 153 mV dec^{-1}, respectively (Figure 5B). The low Tafel slope is indicative of effective communication between MWCNTs and nickel nanoparticles. It facilitated faster kinetics of the OER reaction. The electrode showed the good stability at an onset potential of 0.7 V versus Ag/AgCl with a current density of 10 mA cm^{-2} at 30 °C for 8 h on graphite paper. The data are presented versus RHE along with the normalized current density in Figure 5D. Nickel is the excellent HER catalyst, and its performance for hydrogen generation was evaluated by recording LSV in negative potential as shown in Figure 5A. The electrode showed the onset potential of 145 mV, lower than the Ni@C reported in the literature, and low Tafel slope (166 mV dec^{-1}).[10,18,25] It signifies the presence of metallic nickel which was confirmed by powder XRD as shown in Figure 1, as an active species for HER reaction. Here, we are also anticipating the presence of an intermediate oxidation state which can cleave the adsorbed H_2O_{ad} molecule into an adsorbed OH^-_{ad} and H atom. The preferential recombination of H atom generates H_2 by Volmer process. The stability of the electrode was evaluated at a potential of −1.4 V versus RHE at 35 mA cm^{-2} current density for 14 h for HER (Figure 5C). The constant current indicated the excellent stability of the electrode for HER activity. The calculated electrochemically active surface area (ECSA) was 0.0375 cm^2 (Figure S2) which was directly proportional to the electrochemical double layer capacitance (Cdl). The calculated turn over frequency (TOF) was found to be 0.035 s^{-1} for OER and 0.094 s^{-1} for HER at 350 mV. It is much higher when compared to the NiCo-LDH nanosheets.[50]

After electrochemical stability, Ni@MWCNT was subjected to post morphological characterization. The coated catalyst on graphite paper was scraped and removed by ultrasonication. The intact Ni in MWCNT suggests its excellent stability (TEM images, Figure S3). It was supported from the PXRD data (Figure S4), and SEM images and their corresponding elemental composition. A close look at the elemental composition revealed that the atomic percentage of Ni was

https://doi.org/10.1021/acsomega.2c00070
ACS Omega 2022, 7, 15467−15477

found to be increased after HER stability (Figure S5), whereas after OER stability decrease in atomic percentage of Ni and increase in atomic percentage of oxygen was observed (Figure S6). This indicates that there may be possible formation of NiO/NiOOH during the OER activity (Figure S6). The XPS spectra of Ni@MWCNT after OER stability further supported the coexistence of Ni^{2+}/Ni^{3+} peaks at 856 eV (Figure S7). An identical peak was also observed in XPS spectra of Ni@MWCNT after HER stability study (Figure S8).

After evaluation of electrochemical properties of Ni@MWCNT, we made a membrane electrode assembly (MEA) and demonstrated its alkaline water splitting ability in electrolysis cell. MEA was constructed from *N*-methyl piperidone-based membrane and nickel foam-coated Ni@MWCNT. Membrane preparation detail is provided in the experimental section and its schematics is presented in Figure 6. It is a thermoset anion exchange membrane prepared by the thermal annealing of NMPi-formaldehyde prepolymer and PVA followed by the quaternization with methyl iodide (Figure 6A). The in situ addition of tetraethyl orthosilicate and zirconium oxychloride results into the formation of composite membranes. We have prepared three membranes, namely, NMPi, SiO_2-NMPi, and ZrO_2-NMPi. Figure 6B display the photographs of the synthesized membranes. The prepolymer used for the preparation of three membrane have been characterized by NMR and data are presented in Supporting Information (Figure S9). Figure 7A shows the recorded XRD spectra of membranes. In all three membranes, two characteristic peaks were observed for PVA at ∼20° and ∼40°. They were assigned (101) and (111) planes, respectively.[51] SiO_2-NMPi membrane shows peaks around 22° for amorphous SiO_2 (111).[52] The peaks at ∼30°, 35° for ZrO_2-NMPi membrane were assigned to the tetragonal structure of ZrO_2 with plane (101), (110).[53] Further confirmation was supported by FTIR spectra (Figure 7B). The presence of a broad peak at ∼3550 cm^{-1} shows O−R stretching of PVA in all three membranes. The peaks at 2000 and 1845 cm^{-1} represent the O−Si stretching of SiO_2. The synthesized ZrO_2-NMPi membrane shows an additional peak at 1633 cm^{-1} due to the stretching of Zr−O bond. Figure 7C shows the UTM analysis of the membranes. Obtained tensile stress versus tensile strain plot shows the ZrO_2-NMPi membrane with 87.5% elongation break which is greater than 73.95% for SiO_2-NMPi and 20% for NMPi membrane. The addition of SiO_2 and ZrO_2 increases the Young's modulus of the membranes. The obtained values were 93, 75, and 46 MPa for ZrO_2-NMPi, SiO_2-NMPi, and NMPi, respectively. The formation of dense membrane was observed from SEM analysis (Figure S10). The membranes were found to be crack free and no phase separation and aggregation was observed. There was uniform distribution of SiO_2 and ZrO_2 particles throughout the membrane. The addition of SiO_2 and ZrO_2 have a notable effect on the thermal stability of the membrane. Figure 8A shows the recorded TGA curves in inert atmosphere. All three membranes showed three step weight loss. The initial weight loss at ∼150 °C was due to the loss of adsorbed water molecules. But of the three membranes, the membrane with high water content showed high weight loss. The second weight loss at 220−350 °C was due to the partial degradation of functional groups present in the membrane. The weight loss above 400 °C was due to degradation of a polymer backbone. Before performing the water electrolysis experiments, electro- and physicochemical properties of the membranes were evaluated and presented in Table 1. Of the three membranes, ZrO_2-NMPi showed the highest IEC, water

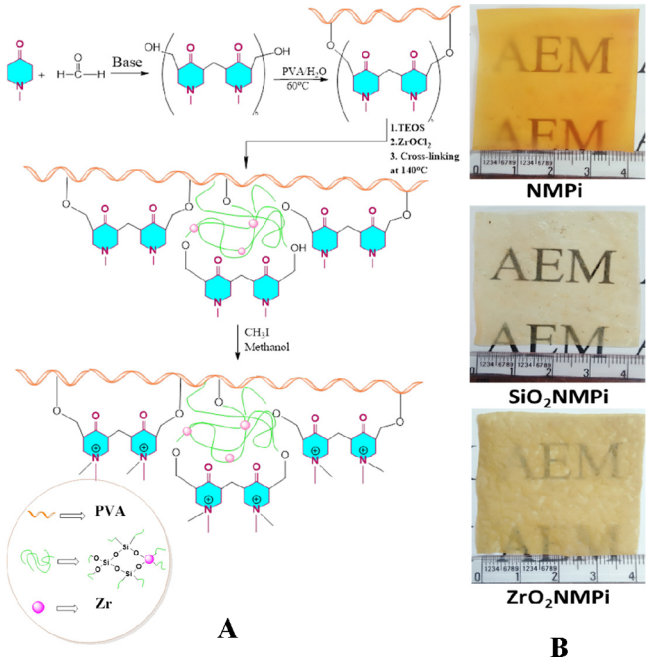

Figure 6. (A) Schematics of composite anion exchange membrane. (B) Photograph of the prepared membranes.

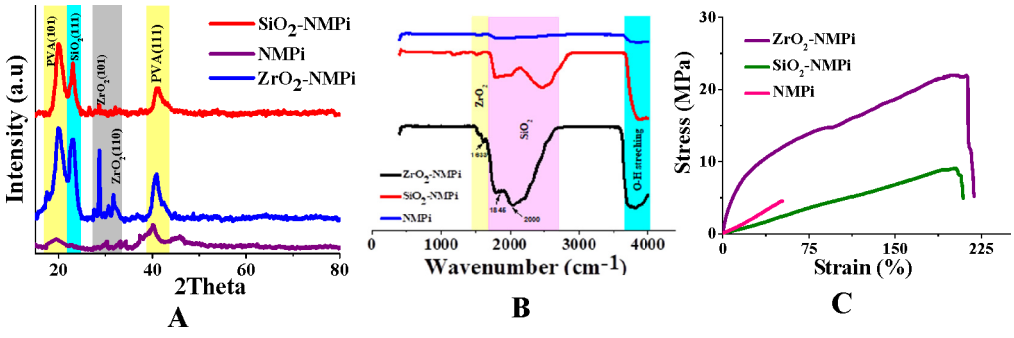

Figure 7. (A) XRD spectra of membranes confirming the presence of SiO_2 and ZrO_2 in the membrane matrix. (B) FTIR spectra to support the presence of SiO_2 and ZrO_2 in the membrane matrix. (C) UTM analysis of the membrane displaying the SiO_2- and ZrO_2-dependent elongation at break.

https://doi.org/10.1021/acsomega.2c00070
ACS Omega 2022, 7, 15467−15477

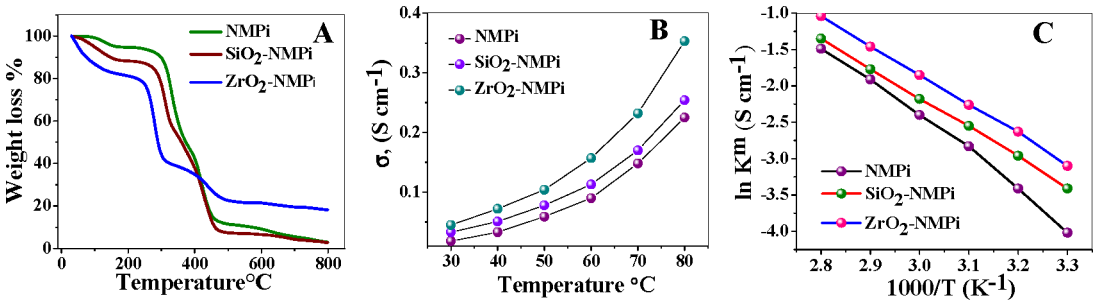

Figure 8. (A) TGA showing two step degradation of NMPi, SiO_2-NMPi and ZrO_2-NMPi membranes. (B) Graph showing calculated conductivity of membranes at the different temperature. (C) Corresponding Arrhenius plot of the membranes.

Table 1. Electro- and Physicochemical Properties of the Different Membrane

Sr. No.	membrane	IEC (meq g^{-1})	water uptake (%)	areal resistance in 0.5 M KOH, Ω cm^{-2} at 50 °C	transport number in 0.5 M NaCl	activation energy (E_a, kJ mol^{-1})	Young modulus (MPa)
1	NMPi	1.89	45.40	16.94	0.72	16.47	46
2	SiO_2-NMPi	2.41	47.20	12.82	0.89	11.72	75
3	ZrO_2-NMPi	2.80	51.30	9.61	0.91	10.13	93

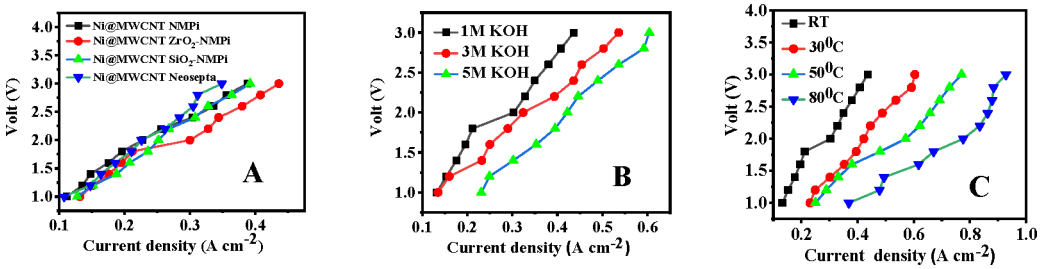

Figure 9. Polarization curve recorded for the membrane electrode assembly with NMPi, ZrO_2-NMPi, SiO_2-NMPi, and Neosepta membranes. (A) Ni@MWCNT/NF with different membranes in 1 M KOH at room temperature. (B) Ni@MWCNT/NF with ZrO_2-NMPi membrane in various concentration of KOH at room temperature. (C) Ni@MWCNT/NF with ZrO_2-NMPi membrane in 5 M KOH at different temperatures.

content, and transport number and low resistance due to the affinity of ZrO_2 to the hydroxyl ions.

Membrane Electrode Assembly. The assembly of the MEA is presented in Figures S11 and S12. The performance was evaluated in a two-compartment cell used for redox flow battery in recirculation mode at constant voltage, and corresponding current was recorded with the help of constant voltage power supply (accuracy voltage ±10 mV and current ±0.1 mA). ZrO_2-NMPi membrane showed relatively high current density value compared to SiO_2-NMPi, NMPi, and commercial Neosepta membranes at constant applied potential. This observation may be explained by its high conductivity (4.5×10^{-2} S cm^{-1}) and low activation energy (10.127 kJ mol^{-1}) in comparison with SiO_2-NMPi ($K = 3.3 \times 10^{-2}$ S cm^{-1} and E_a = 11.718 kJ mol^{-1}) and NMPi ($K = 1.8 \times 10^{-2}$ S cm^{-1} and E_a = 16.474 kJ mol^{-1}) (Figure 8B,C). The recorded polarization curves presented in Figure 9A show three well-defined regions. The first linear region of 1.0−1.8 V corresponded to the activation overpotential for activation energy of formation of hydrogen and oxygen on the electrode surface. The second region of 1.8 to 2.2 V can be attributed to ohmic overpotential comprising resistance of all components of the cell, that is, ohmic resistance of electrodes, current collectors, resistance incurred from gas bubble formation, ionic resistance of electrolyte, resistivity of membrane, and so forth. The third region of 2.2−3.0 V can be considered as the concentration overpotential due to the resistance to the mass transport at the electrode surface at high current density. The assembled Ni@MWCNT electrocatalyst with ZrO_2-NMPi, SiO_2-NMPi, and NMPi membrane electrode assembly shows high current density of 300, 252, and 228 mA cm^{-2}, respectively, at room temperature in 1 M KOH at 2.00 V constant potential. With an increase in concentration of KOH (Figure 9B) and temperature (Figure 9C) current density was also increased. The maximum current density of 776 mA cm^{-2} was obtained in 5 M KOH at 80 °C (Figure 9C) with ZrO_2-NMPi membrane. The calculated faradic efficacy of the water splitting was 94.33% higher for ZrO_2-NMPi membrane followed by 80.23% SiO_2-NMPi, 77.7% NMPi, and 65.10% Neosepta membranes. The results are comparatively better than a commercially available Neosepta membrane in identical experimental conditions. The Neosepta membrane showed 245 mA cm^{-2} current density at 2.00 V in 1 M KOH at room temperature (Figure 9A). The stability of the best membrane ZrO_2-NMPi was evaluated in 1 M KOH at onset potential of 2 V at room temperature. Figure 10 shows the obtained constant current over 24 h experiment. For the comparison purpose, data for Neosepta membrane is also presented in Figure 10. From the Figure 10, it is clear that performance of ZrO_2-NMPi is far better than a Neosepta membrane. At 2 V, it gave a current density of 300 mA cm^{-2}, whereas a Neosepta membrane gave a current density of 197 mA cm^{-2}. These data are comparable with the literature reported in Table 2 with different types of membranes. The values of current

https://doi.org/10.1021/acsomega.2c00070
ACS Omega 2022, 7, 15467−15477

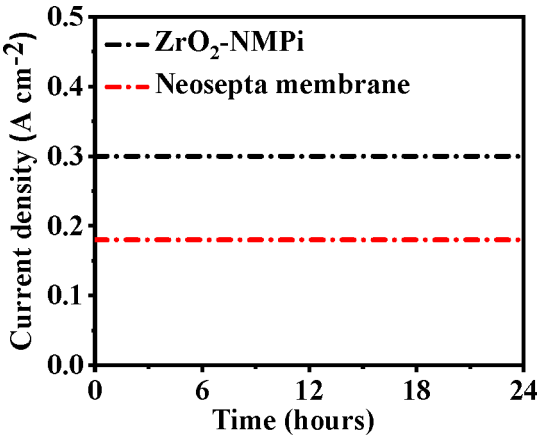

Figure 10. Stability of the MEA assembled with ZrO_2-NMPi membrane in 1 M KOH and onset voltage of 2 V at room temperature (25 °C).

density, operating conditions, and catalysts used are also presented in Table 2. Of the reported membranes, polybenzimidazole, Aemion, and Sustainion have better performances than ZrO_2-NMPi. The other membranes showed poor performance indicating the best utility of the newly synthesized Ni@MWCNT electrocatalyst and ZrO_2-NMPi membrane for hydrogen generation and/or related other applications. After stability study, the SEM images of ZrO_2-NMPi and SiO_2-NMPi membranes were recorded, and we found that there is no leaching of silica which was confirmed by energy dispersive X-ray spectrum (Figure S13).

CONCLUSION

In summary, we have successfully developed bifunctional (OER and HER) nickel nanoparticle-encapsulated MWCNT electrocatalysts that were used in MEA with ZrO_2-NMPi membrane for alkaline water electrolysis. The encapsulated material showed excellent water splitting performance in alkaline medium with current density of 10 mA cm^{-2} at lower potential of 254 mV for HER and 300 mV for OER. An MEA was assembled with ZrO_2-NMPi membrane and Ni@MWCNT electrocatalyst and performed the water splitting experiments. A current density of 776 mA cm^{-2} at 80 °C in 5 M KOH was achieved which is comparable with literature of known noble metal catalysts and better than non-noble metal catalysts. Thus, facile preparation of anion exchange membrane and bifunctional Ni@MWCNT electrocatalyst suggests their potential utility in hydrogen generation applications.

ASSOCIATED CONTENT

Supporting Information

The Supporting Information is available free of charge at https://pubs.acs.org/doi/10.1021/acsomega.2c00070.

Physicochemical and electrochemical characterization of the synthesized membranes; water uptake, ion exchange capacity (IEC), transport number; faradaic efficiency; supporting figure include isotherm linear plots of Ni@MWCNT and neat nickel; cyclic voltammetry curves of Ni@MWCNT at different scan rate and the capacitive current versus scan rate (mV s^{-1}) plot for Ni@MWCNT; TEM images of Ni@MWCNTs after stability test; XRD patterns of Ni@MWCNTs/GP after stability test; SEM image along with EDX elemental analysis of Ni@MWCNTs after stability test; XPS spectra of Ni@MWCNT after stability test; ^1H NMR and C^{13} NMR spectra of NMP monomer; SEM image along with EDX elemental analysis of ZrO_2-NMPi, SiO_2-NMPi membrane, NMPi membrane; photograph of membrane electrode assembly; photographs of different components of alkaline water electrolyzer; after stability SEM image along with EDX elemental analysis of ZrO_2-NMPi, SiO_2-NMPi membrane; supporting table includes comparison table of electrochemical properties of Ni@MWCNT electro-catalyst with literature (PDF)

AUTHOR INFORMATION

Corresponding Author

Rajaram K. Nagarale − *Electro Membrane Processes Laboratory, Membrane Science and Separation Technology Division, CSIR-Central Salt and Marine Chemicals Research Institute, Bhavnagar 364002, India; Academy of Scientific and Innovative Research (AcSIR), Ghaziabad 201002, India;* orcid.org/0000-0002-9742-8104; Email: rknagarale@csmcri.org

Table 2. Reported Literature Values of Electrolysis Performance of MEA[a]

membranes	catalyst (anode and cathode)	experimental condition	electrolysis performance	references
membrane-free	Co_3O_4/NrGO with IrO_2	1 M KOH	1.9 V at 199 mA cm^{-2}	54
PBI membrane	nanoparticle IrO_2 catalyst on a GDE	1 M KOH	1.09 V at 1000 mA cm^{-2}	55
HTMA-DAPP	NiFe nanofoam and $Pt_{0.5}Ru_{0.25}$/C	1 M NaOH solution at 60 °C	2.7 A cm^{-2} at 1.8 V	56
PSEBS-CM-DABCO	$NiFe_2O_4$ and $NiCo_2O_4$	15 wt % KOH solution at 40 °C	2.0 V at 150 mA cm^{-2}	16
TPN1-100	PGM/PGM	1.0 M NaOH solution at 50 °C	2.1 V at 300 mA cm^{-2}	57
SEBS-Pi	Pt/C, carbon and IrO_2, Ni foam	5.6 wt % KOH solution at 50 °C	2.0 V at 400 mA cm^{-2}	36
PAni-1.03	$NiCo_2O_4$-HSp and $NiCo_2O_4$-HSp	1.0 M KOH at 50 °C	2.0 V at 400 mA cm^{-2}	37
ABPBI	nickel foam and nickel foam	3 M KOH solution at 70 °C	2.0 V at 300 mA cm^{-2}	58
QMSV	nickel foam and nickel foam	10 wt % KOH solution at 25 °C	2.8 V at 280 mA cm^{-2}	59
Fumasep FAS-50	Pt/C and Co_3O_4/NiGO	1.0 M KOH at r.t.	∼1.96 V at 400 mA cm^{-2}	54
Aemion	Ir/Pt	1.0 M KOH at 50 °C	1.73 V at 1000 mA cm^{-2}	60
Sustainion	$Cu_{0.5}Co_{2.5}O_4$ and Pt/C	1.0 M KOH at 50 °C	1.75 V at 1000 mA cm^{-2}	61
Zr-SiO_2-NMPi	Ni@MWCNT/Ni@MWCNT	5 M KOH at 80 °C	2.00 V at 776 mA cm^{-2}	present work

[a]Footprint: PBI, polybenzimidazole; HTMA-DAPP, hexyltrimethylammonium-Diels−Alder polyphenylenes; PSEBS, polystyrene-*block*-poly(ethylene-*ran*-butylene)-*block*-polystyrene; DABCO, 1,4-diazabicyclo[2.2.2]octane; TPN1-100, poly(terphenylene); SEBS-Pi, poly(styrene-*b*-(ethylene-*co*-butylene)-*b*-styrene; PAni, polyaniline; QMSV, quaternized poly(styrene-*co*-vinylbenzyl chloride); NMPi, *N*-methyl-4-piperidone

https://doi.org/10.1021/acsomega.2c00070
ACS Omega 2022, 7, 15467−15477

Authors

Dimple K. Bora − *Electro Membrane Processes Laboratory, Membrane Science and Separation Technology Division, CSIR-Central Salt and Marine Chemicals Research Institute, Bhavnagar 364002, India; Academy of Scientific and Innovative Research (AcSIR), Ghaziabad 201002, India; Inorganic Materials and Catalysis Division, CSIR-Central Salt and Marine Chemicals Research Institute, Bhavnagar 364002, India*

Priyanka P. Bavdane − *Electro Membrane Processes Laboratory, Membrane Science and Separation Technology Division, CSIR-Central Salt and Marine Chemicals Research Institute, Bhavnagar 364002, India; Academy of Scientific and Innovative Research (AcSIR), Ghaziabad 201002, India*

Vidhiben Dave − *Electro Membrane Processes Laboratory, Membrane Science and Separation Technology Division, CSIR-Central Salt and Marine Chemicals Research Institute, Bhavnagar 364002, India; Academy of Scientific and Innovative Research (AcSIR), Ghaziabad 201002, India*

Sooraj Sreenath − *Electro Membrane Processes Laboratory, Membrane Science and Separation Technology Division, CSIR-Central Salt and Marine Chemicals Research Institute, Bhavnagar 364002, India; Academy of Scientific and Innovative Research (AcSIR), Ghaziabad 201002, India*

Govind Sethia − *Academy of Scientific and Innovative Research (AcSIR), Ghaziabad 201002, India; Inorganic Materials and Catalysis Division, CSIR-Central Salt and Marine Chemicals Research Institute, Bhavnagar 364002, India*

Ashis Kumar Satpati − *Analytical Chemistry Division, Bhabha Atomic Research Centre, Mumbai 400085, India;* orcid.org/0000-0002-2732-8706

Complete contact information is available at: https://pubs.acs.org/10.1021/acsomega.2c00070

Notes

The authors declare no competing financial interest.

■ ACKNOWLEDGMENTS

R.K.N. thank you for the financial support (Grant Number 58/14/22/2019-BRNS) from Board of Research in Nuclear Sciences, Department of Atomic Energy (DAE); Government of India and CSIR institute project funding (MLP-0063). Director CSIR-CSMCRI is acknowledged for continuous support and encouragement. Instrumentation facilities provided by the Analytical Discipline and Centralized Instrument Facility, CSIR-CSMCRI, Bhavnagar, are gratefully acknowledged. CSIR-CSMCRI manuscript number 247/2021.

■ REFERENCES

(1) Chen, H.; Liu, Y.; Zhang, B.; Zou, X. Future directions of catalytic chemistry. *Pure Appl. Chem.* **2021**, *93*, 1411−1421.

(2) Wang, Y.; Li, X.; Zhang, M.; Zhang, J.; Chen, Z.; Zheng, X.; Tian, Z.; Zhao, N.; Han, X.; Zaghib, K.; Wang, Y.; Deng, Y.; Hu, W. Highly Active and Durable Single-Atom Tungsten-Doped $NiS_{0.5}Se_{0.5}$ Nanosheet@$NiS_{0.5}Se_{0.5}$ Nanorod Heterostructures for Water Splitting. *Adv. Mater.* **2022**, *34*, 2107053.

(3) Wang, H.; Yuan, Y.; Gu, J.; Jia, Z.; Lu, Z.; Bai, Z.; Yang, L.; Yang, X. Facile one-pot synthesis of layered double hydroxides nanosheets with oxygen vacancies grown on carbon nanotubes for efficient oxygen evolution reaction. *Chem. Eng. J.* **2022**, *430*, 132623.

(4) Jiang, R.; Da, Y.; Chen, Z.; Cui, X.; Han, X.; Ke, H.; Liu, Y.; Chen, Y.; Deng, Y.; Hu, W. Progress and Perspective of Metallic Glasses for Energy Conversion and Storage. *Adv. Energy Mater.* **2022**, *12*, 2101092.

(5) Li, J.; Liu, Y.; Chen, H.; Zhang, Z.; Zou, X. Design of a Multilayered Oxygen-Evolution Electrode with High Catalytic Activity and Corrosion Resistance for Saline Water Splitting. *Adv. Funct. Mater.* **2021**, *31*, 2101820.

(6) Kubacka, A.; Fernández-García, M.; Colón, G. Advanced nanoarchitectures for solar photocatalytic applications. *Chem. Rev.* **2012**, *112*, 1555−1614.

(7) Xi, W.; Ren, Z.; Kong, L.; Wu, J.; Du, S.; Zhu, J.; Xue, Y.; Meng, H.; Fu, H. Dual-valence nickel nanosheets covered with thin carbon as bifunctional electrocatalysts for full water splitting. *J. Mater. Chem. A* **2016**, *4*, 7297−7304.

(8) Yang, Y.; Liu, J.; Guo, S.; Liu, Y.; Kang, Z. A nickel nanoparticle/carbon quantum dot hybrid as an efficient electrocatalyst for hydrogen evolution under alkaline conditions. *J. Mater. Chem. A* **2015**, *3*, 18598−18604.

(9) Carmo, M.; Fritz, D. L.; Mergel, J.; Stolten, D. A comprehensive review on PEM water electrolysis. *Int. J. Hydrog. Energy.* **2013**, *38*, 4901−4934.

(10) Maiyalagan, T.; Jarvis, K. A.; Therese, S.; Ferreira, P. J.; Manthiram, A. Spinel-type lithium cobalt oxide as a bifunctional electrocatalyst for the oxygen evolution and oxygen reduction reactions. *Nat. Commun.* **2014**, *5*, 3949.

(11) Wang, H.; Lee, H.-W.; Deng, Y.; Lu, Z.; Hsu, P.-C.; Liu, Y.; Lin, D.; Cui, Y. Bifunctional non-noble metal oxide nanoparticle electrocatalysts through lithium-induced conversion for overall water splitting. *Nat. Commun.* **2015**, *6*, 7261.

(12) Stern, L.-A.; Feng, L.; Song, F.; Hu, X. Ni_2P as a Janus catalyst for water splitting: the oxygen evolution activity of Ni_2P nanoparticles. *Energy Environ. Sci.* **2015**, *8*, 2347−2351.

(13) Man, I. C.; Su, H.-Y.; Calle-Vallejo, F.; Hansen, H. A.; Martínez, J. I.; Inoglu, N. G.; Kitchin, J.; Jaramillo, T. F.; Nørskov, J. K.; Rossmeisl, J. Universality in Oxygen Evolution Electrocatalysis on Oxide Surfaces. *ChemCatChem.* **2011**, *3*, 1159−1165.

(14) Parsons, R. The rate of electrolytic hydrogen evolution and the heat of adsorption of hydrogen. *Trans. Faraday Soc.* **1958**, *54*, 1053−1063.

(15) Abidat, I.; Bouchenafa-Saib, N.; Habrioux, A.; Comminges, C.; Canaff, C.; Rousseau, J.; Napporn, T. W.; Dambournet, D.; Borkiewicz, O.; Kokoh, K. B. Electrochemically induced surface modifications of mesoporous spinels (Co_3O_4-δ, $MnCo_2O_4$-δ, $NiCo_2O_4$-δ) as the origin of the OER activity and stability in alkaline medium. *J. Mater. Chem. A* **2015**, *3*, 17433−17444.

(16) Hu, C.; Zhang, L.; Gong, J. Recent progress made in the mechanism comprehension and design of electrocatalysts for alkaline water splitting. *Energy Environ. Sci.* **2019**, *12*, 2620−2645.

(17) Suen, N. T.; Hung, S. F.; Quan, Q.; Zhang, N.; Xu, Y. A.-O.; Chen, H. M. Electrocatalysis for the oxygen evolution reaction: recent development and future perspectives. *Chem. Soc. Rev.* **2017**, *46*, 337−365.

(18) Zhang, X.; Liang, Y. Nickel Hydr(oxy)oxide Nanoparticles on Metallic MoS_2 Nanosheets: A Synergistic Electrocatalyst for Hydrogen Evolution Reaction. *Adv. Sci.* **2018**, *5*, 1700644.

(19) Ren, J.; Antonietti, M.; Fellinger, T.-P. Electrocatalysts: Efficient Water Splitting Using a Simple Ni/N/C Paper Electrocatalyst. *Adv. Energy Mater.* **2015**, *5*, 1401660.

(20) Liu, X.; Liu, W.; Ko, M.; Park, M.; Kim, M. G.; Oh, P.; Chae, S.; Park, S.; Casimir, A.; Wu, G.; Cho, J. Metal (Ni, Co)-Metal Oxides/Graphene Nanocomposites as Multifunctional Electrocatalysts. *Adv. Funct. Mater.* **2015**, *25*, 5799−5808.

(21) Yan, X.; Gu, M.; Wang, Y.; Xu, L.; Tang, Y.; Wu, R. In-situ growth of Ni nanoparticle-encapsulated N-doped carbon nanotubes on carbon nanorods for efficient hydrogen evolution electrocatalysis. *Nano. Res.* **2020**, *13*, 975−982.

(22) Yang, L.; Zhou, W.; Jia, J.; Xiong, T.; Zhou, K.; Feng, C.; Zhou, J.; Tang, Z.; Chen, S. Nickel nanoparticles partially embedded into carbon fiber cloth via metal-mediated pitting process as flexible and

efficient electrodes for hydrogen evolution reactions. *Carbon* **2017**, *122*, 710−717.
(23) Lei, C.; Wang, Y.; Hou, Y.; Liu, P.; Yang, J.; Zhang, T.; Zhuang, X.; Chen, M.; Yang, B.; Lei, L.; Yuan, C.; Qiu, M.; Feng, X. Efficient alkaline hydrogen evolution on atomically dispersed Ni−Nx Species anchored porous carbon with embedded Ni nanoparticles by accelerating water dissociation kinetics. *Energy Environ. Sci.* **2019**, *12*, 149−156.
(24) Chhetri, M.; Sultan, S.; Rao, C. N. R. Electrocatalytic hydrogen evolution reaction activity comparable to platinum exhibited by the $Ni/Ni(OH)_2$/graphite electrode. *Proc. Natl. Acad. Sci. U. S. A.* **2017**, *114*, 8986−8990.
(25) Agegnehu, A. K.; Pan, C.-J.; Rick, J.; Lee, J.-F.; Su, W.-N.; Hwang, B.-J. Enhanced hydrogen generation by cocatalytic Ni and NiO nanoparticles loaded on graphene oxide sheets. *J. Mater. Chem.* **2012**, *22*, 13849−13854.
(26) Ajayan, P. M.; Lijima, S. Capillarity-induced filling of carbon nanotubes. *Nature* **1993**, *361*, 333−334.
(27) Takenobu, T.; Takano, T.; Shiraishi, M.; Murakami, Y.; Ata, M.; Kataura, H.; Achiba, Y.; Iwasa, Y. Stable and controlled amphoteric doping by encapsulation of organic molecules inside carbon nanotubes. *Nat. Mater.* **2003**, *2*, 683−688.
(28) Zou, R.; Zhang, Z.; Liu, Q.; Xu, K.; Lu, A.; Hu, J.; Li, Q.; Bando, Y.; Golberg, Z. Melting of Metallic Electrodes and Their Flowing Through a Carbon Nanotube Channel within a Device. *Adv. Mater.* **2013**, *25*, 2693−2699.
(29) Gimenez-Lopez, M. C.; Chuvilin, A.; Kaiser, U.; Khlobystov, A. N. Functionalised endohedral fullerenes in single-walled carbon nanotubes. *ChemComm.* **2011**, *47*, 2116−2118.
(30) Smith, B. W.; Monthioux, M.; Luzzi, D. E. Encapsulated C60 in carbon nanotubes. *Nature* **1998**, *396*, 323−324.
(31) Rajapakse, M.; Karki, B.; Abu, U. O.; Pishgar, S.; Musa, M. R. K.; Riyadh, S. M. S.; Yu, M.; Sumanasekera, G.; Jasinski, J. B. Intercalation as a versatile tool for fabrication, property tuning, and phase transitions in 2D materials. *NPJ. 2D Mater. Appl.* **2021**, *5*, 30.
(32) Kataura, H.; Maniwa, Y.; Abe, M.; Fujiwara, A.; Kodama, T.; Kikuchi, K.; Imahori, H.; Misaki, Y.; Suzuki, S.; Achiba, Y. Optical properties of fullerene and non-fullerene peapods. *Appl. Phys. A: Mater. Sci. Process.* **2002**, *74*, 349−354.
(33) Simon, F.; Monthioux, M. Fullerenes inside Carbon Nanotubes: The Peapods. *Carbon Meta-Nanotubes* **2011**, 273−321.
(34) Ugarte, D.; Chatelain, A.; de Heer, W. A. Nanocapillarity and Chemistry in Carbon Nanotubes. *Science* **1996**, *274*, 1897−1899.
(35) Sreenath, S.; Suman, R.; Sayana, K. V.; Nayanthara, P. S.; Borle, N. G.; Verma, V.; Nagarle, R. K. Low-Voltage Nongassing Electroosmotic Pump and Infusion Device with Polyoxometalate-Encapsulated Carbon Nanotubes. *Langmuir.* **2021**, *37*, 1563−1570.
(36) Su, X.; Gao, L.; Hu, L.; Qaisrani, N. A.; Yan, X.; Zhang, W.; Jiang, X.; Ruan, X.; He, G. Novel piperidinium functionalized anionic membrane for alkaline polymer electrolysis with excellent electrochemical properties. *J. Membr. Sci.* **2019**, *581*, 283−292.
(37) Bhushan, M.; Mani, M.; Singh, A. K.; Panda, A. B.; Shahi, V. K. Self-standing polyaniline membrane containing quaternary ammonium groups loaded with hollow spherical NiCo2O4 electrocatalyst for alkaline water electrolyser. *J. Mater. Chem. A* **2020**, *8*, 17089−17097.
(38) Cheng, J.; Zhang, X.; Ye, Y. Synthesis of nickel nanoparticles and carbon encapsulated nickel nanoparticles supported on carbon nanotubes. *J. Solid State Chem.* **2006**, *179*, 91−95.
(39) Chen, D.-H.; Hsieh, C.-H. Synthesis of nickel nanoparticles in aqueous cationic surfactant solutions. *J. Mater. Chem.* **2002**, *12*, 2412−2415.
(40) Koltypin, Y.; Fernandez, A.; Rojas, T. C.; Campora, J.; Palma, P.; Prozorov, R.; Gedanken. Encapsulation of Nickel Nanoparticles in Carbon Obtained by the Sonochemical Decomposition of $Ni(C_8H_{12})_2$. *Chem. Mater.* **1999**, *11*, 1331−1335.
(41) Sharma, S. K.; Vastola, F. J.; Walker, P. L. Reduction of nickel oxide by carbon: III. Kinetic studies of the interaction between nickel oxide and natural graphite. *Carbon* **1997**, *35*, 535−534.
(42) Cullity, B. D. *Elements of X-Ray Diffraction*, 2nd ed; Academic Press, 1978; pp 1−569.
(43) Payne, B. P.; Biesinger, M. C.; McIntyre, N. S. The study of polycrystalline nickel metal oxidation by water vapour. *J. Electron Spectrosc. Relat. Phenom.* **2009**, *175*, 55−65.
(44) Lu, Q. H.; Huang, R.; Wang, L. S.; Wu, Z. G.; Li, C.; Luo, Q.; Zuo, S. Y.; Li, J.; Peng, D. L.; Han, G. L.; Yan, P. X. Thermal annealing and magnetic anisotropy of NiFe thin films on n+-Si for spintronic device applications. *J. Magn. Magn. Mater.* **2015**, *394*, 253−259.
(45) Wagner, C. D.; Gale, L. H.; Raymond, R. H. Two-dimensional chemical state plots: a standardized data set for use in identifying chemical states by X-ray photoelectron spectroscopy. *Anal. Chem.* **1979**, *51*, 466−482.
(46) Moulder, J. F.; Stickle, W. F.; Sobol, W. M.; Bomben, K. D. *Handbook of X-Ray Photoelectron Spectroscopy*. Academic Press, 1992; pp 1−261.
(47) Riyajuddin, S.; Azmi, K.; Pahuja, M.; Kumar, S.; Maruyama, T.; Bera, C.; Ghosh, K. Super-Hydrophilic Hierarchical Ni-Foam-Graphene-Carbon Nanotubes-Ni_2P-CuP_2 Nano-Architecture as Efficient Electrocatalyst for Overall Water Splitting. *ACS Nano* **2021**, *15*, 5586−5599.
(48) Subbaraman, R.; Tripkovic, D.; Chang, K.-C.; Strmcnik, D.; Paulikas, A. P.; Hirunsit, P.; Chan, M.; Greeley, J.; Stamenkovic, V.; Markovic, N. M. Trends in activity for the water electrolyser reactions on 3d M(Ni,Co,Fe,Mn) hydr(oxy)oxide catalysts. *Nat. Mater.* **2012**, *11*, 550−557.
(49) Nagarale, R. K.; Hoss, U.; Heller, A. Mixed-Valence Metal Oxide Nanoparticles as Electrochemical Half-Cells: Substituting the Ag/AgCl of Reference Electrodes by CeO_2−x Nanoparticles. *J. Am. Chem. Soc.* **2012**, *134*, 20783−20787.
(50) Jiang, J.; Zhang, A.; Li, L.; Ai, L. Nickel-cobalt layered double hydroxide nanosheets as high-performance electrocatalyst for oxygen evolution reaction. *J. Power Sources.* **2015**, *278*, 445−451.
(51) Tang, C.-M.; Tian, Y.-H.; Hsu, S.-H. Poly(vinyl alcohol) Nanocomposites Reinforced with Bamboo Charcoal Nanoparticles: Mineralization Behavior and Characterization. *Materials* **2015**, *8*, 4895−4911.
(52) Yang, L. Y.; Li, H. Z.; Liu, J.; Sun, Z. Q.; Tang, S. S.; Lei, M. Dual yolk-shell structure of carbon and silica-coated silicon for high-performance lithium-ion batteries. *Sci. Rep.* **2015**, *5*, 10908.
(53) Fang, D.; Huang, K.; Luo, Z.; Wang, Y.; Liu, S.; Zhang, Q. Freestanding ZrO_2 nanotube membranes made by anodic oxidation and effect of heat treatment on their morphology and crystalline structure. *J. Mater. Chem.* **2011**, *21*, 4989−4994.
(54) Vineesh, T. V.; Sekar, A.; Rajappa, S.; Pal, S.; Alwarappan, S.; Narayanan, T. N. Non-Precious Metal/Metal Oxides and Nitrogen-Doped Reduced Graphene Oxide based Alkaline Water-Electrolysis Cell. *ChemCatChem.* **2017**, *9*, 4295−4300.
(55) Kaczur, J.; Yang, H.; Liu, Z.; Masel, R. Carbon Dioxide and Water Electrolysis Using New Alkaline Stable Anion Membranes. *Front. Chem.* **2018**, DOI: 10.3389/fchem.2018.00263.
(56) Li, D.; Park, E. J.; Zhu, W.; Shi, Q.; Zhou, Y.; Tian, H.; Lin, Y.; Serov, A.; Zulevi, B.; Baca, E. D.; Fujimoto, C.; Chung, H. T.; Kim, Y. S. Highly quaternized polystyrene ionomers for high performance anion exchange membrane water electrolysers. *Nat. Energy.* **2020**, *5*, 378−385.
(57) Park, E. J.; Capuano, C. B.; Ayers, K. E.; Bae, C. Chemically durable polymer electrolytes for solid-state alkaline water electrolysis. *J. Power Sources.* **2018**, *375*, 367−372.
(58) Diaz, L. A.; Hnát, J.; Heredia, N.; Bruno, M. M.; Viva, F. A.; Paidar, M.; Corti, H. R.; Bouzek, K.; Abuin, G. C. Alkali doped poly (2,5-benzimidazole) membrane for alkaline water electrolysis: Characterization and performance. *J. Power Sources.* **2016**, *312*, 128−136.
(59) Vengatesan, S.; Santhi, S.; Jeevanantham, S.; Sozhan, G. Quaternized poly (styrene-co-vinylbenzyl chloride) anion exchange membranes for alkaline water electrolysers. *J. PowerSources.* **2015**, *284*, 361−368.

https://doi.org/10.1021/acsomega.2c00070
ACS Omega 2022, 7, 15467−15477

(60) Fortin, P.; Khoza, T.; Cao, X.; Martinsen, S. Y.; Barnett, A. O.; Holdcroft, S. High-performance alkaline water electrolysis using Aemion anion exchange membranes. *J. PowerSources.* **2020**, *451*, 227814.
(61) Zignani, S.; Faro, M. L.; Trocino, S.; Aricò, A. Investigation of NiFe-Based Catalysts for Oxygen Evolution in Anion-Exchange Membrane Electrolysis. *Energies* **2020**, *13*, 1720.

https://doi.org/10.1021/acsomega.2c00070
ACS Omega 2022, 7, 15467−15477